Effects of Temperature on Flow Fouling of Smooth and Nonwetting Surfaces

S. Hatte and R. Pitchumani*

Advanced Materials and Technologies Laboratory

Department of Mechanical Engineering

Virginia Tech, Blacksburg, Virginia 24061-0238, United States

ABSTRACT

This paper presents a comparative study of temperature-dependent mineral fouling deposition on smooth surface and nonwetting superhydrophobic and lubricant-infused surfaces under dynamic flow conditions. The surfaces are represented in a unified manner using the viscosity ratio of the infused material within the porous asperities on a surface to that of the flowing fluid, such that the spectrum of surfaces from superhydrophobic to smooth is captured by the range of viscosity ratio from 0 to ∞. Using a forced convection experimental setup, deposition of calcium sulfate on the surfaces is quantified in terms of asymptotic fouling resistance over a range of temperature, Reynolds number and mineral foulant supersaturation. Through a systematic set of accelerated fouling experiments, an analytical relationship for the asymptotic fouling resistance is developed in terms of Reynolds number, foulant concentration, temperature, and surface type. The model is validated with a comprehensive set of experimental data from this study as well as from the literature. Optimum nonwetting surface designs for minimizing fouling resistance compared to conventional smooth surfaces are developed as a function of temperature. The results of the study offer insight into the temperature-dependent fouling of surfaces under flow conditions and a rational design of fouling-resistant nonwetting surfaces that can be readily translated to practice.

KEYWORDS: temperature-dependent fouling; nonwetting surfaces; heat transfer; optimal design; calcium sulfate; analytical model.

* Author for correspondence: pitchu@vt.edu

1. INTRODUCTION

In the last few decades, nonwetting surfaces have received significant attention due to their excellent water repellant properties that are fundamental to the improvement of various energy transport processes such as enhanced phase change heat transfer [1-4], enhanced convective heat transfer [5-8], drag reduction [9-13], anti-icing [14,15], etc. Many of these processes at times coexist in an application allowing for significant improvement in the system effectiveness through the use of nonwetting surfaces. For example, industrial condensers exhibit the flow of untreated coolant on the tube side and condensation heat transfer on the shell side. A modified nonwetting surface design on the tube side can lead to drag reduction, enhanced convection heat transfer and fouling mitigation, and a similar surface modification on the shell side can improve the condensation heat transfer coefficient, collectively improving the overall condenser effectiveness [16].

Several energy transport applications involve the flow of untreated coolant or heat transfer fluid that contains various types of mineral salts such as calcium sulfate, calcium carbonate etc., in trace concentrations. Prolonged exposure of heat transfer surfaces to such solutions leads to the gradual deposition of salt particles on the surfaces. With increase in time, the deposits grow in size and spread across the surfaces leading to degradation of heat transfer performance [17]. In addition, the cleaning and maintenance required to periodically remove the foulant deposits from the heat transfer surfaces leads to negative economic impacts and hinders in the continuous operation of the system [16,18]. Nonwetting metallic surfaces, by virtue of their wettability characteristics, can mitigate foulant deposition and are excellent candidates for heat transfer surfaces. As a result, understanding the mechanism of fouling deposition of salts and investigating the fouling mitigation performance of various promising nonwetting surfaces is of fundamental significance that is sought to be studied in this work.

Several studies have been reported on the characterization of the superior fouling mitigation performance of superhydrophobic and lubricant-infused nonwetting surfaces in a quiescent, static foulant solution. However, a majority of these studies are restricted to biofouling [19-22] and very few studies are focused on the case of mineral salt fouling [23,24]. For example, Subramanyam et al. [23] experimentally showed that the silicon oil-infused nonwetting surfaces

showed about 10-fold reduction in calcium sulfate fouling compared to base of smooth surfaces. They attributed this superior performance of lubricant-infused surfaces to the deterrence of foulant adhesion to the infused oil. Jiang et al. [24] also observed a 2/3rd reduction in fouling on superhydrophobic surfaces compared to CuO nanowire superhydrophilic surfaces owing to the extreme lower nucleation density of foulant resulting from the preservation of Cassie state of wettability under the static configuration of foulant solution.

In contrast to the wealth of literature on the other energy transport processes and static fouling on nonwetting surfaces, mineral fouling on nonwetting surfaces under dynamic fluid flow conditions is relatively less studied. Our prior work [25] presented a systematic experimental analysis to elucidate dynamic flow fouling of calcium carbonate and calcium sulfate on smooth, superhydrophobic and liquid-infused surfaces with a range of infused lubricant viscosity. Copper tubes with modified inner surface wettability were subjected to forced convection at different flow rates and fouling salt concentrations. The study reported, for the first time, a closed-form analytical relationship for the asymptotic fouling thermal resistance on the Reynolds number, dimensionless concentration of fouling agent and dimensionless infused liquid viscosity that represents the different surface types in a unified manner. Contour maps of optimum surface designs for minimizing fouling resistance were presented and the study provides the first ever information on designing surfaces for reduced fouling or for estimating the fouling characteristics for a given surface in applications.

Energy systems and chemical process engineering applications often involve operation at elevated temperatures and, therefore, involve dynamic flow fouling over a range of temperature. For nonwetting surfaces to be useful in fouling mitigation in these applications, the fouling mitigation characteristics need to be understood at the elevated temperatures. Although lubricant-infused nonwetting surfaces were shown to minimize fouling in our previous work [25], the study was limited to fouling at room temperature, and no study exists on the temperature-dependent mineral scaling of nonwetting surfaces in dynamic flow environment.

The present study addresses the aforementioned knowledge gap through a systematic study of calcium sulfate fouling on smooth, superhydrophobic and lubricant-infused surfaces in a unified manner. Nonwetting surfaces are fabricated by a facile process and their wettability

characteristics are measured. A forced convection heat transfer setup is used to quantify the extent of fouling onto heat transfer surfaces in terms of an asymptotic fouling resistance. Representing smooth, superhydrophobic and lubricant-infused surfaces using a single parameter, the viscosity ratio of the lubricant/material infused in the solid surface to that of the flowing fluid, the fouling performance of the different surface types is analyzed in terms of the viscosity ratio. In addition to the surface type, a systematic set of experiments is performed to develop a functional dependence of the asymptotic fouling resistance with the governing parameters namely, Reynolds number, foulant concentration and temperature along with the surface type as defined by the viscosity ratio. It is shown that the unified mathematical formulation developed in the present study predicts the experimental values of asymptotic fouling resistance to within 10% at 90% confidence. Complementing the quantitative characterization of fouling, scanning electron microscope images are presented to elucidated foulant interaction with the various surface types.

The experimental methods are briefly discussed in the next section, followed by the presentation and discussion of results in section 3. The principal conclusions of the study are summarized in section 4.

2. EXPERIMENTAL METHODS

The experimental materials and methods follow those reported in [25] and are briefly outlined here. Copper tubes of inner diameter 7.9 mm and wall thickness 0.8 mm were used in the fouling experiments. As-purchased tubes were used without modification as the reference conventional smooth tubes. For studying fouling of nonwetting surfaces, the inner surface of copper tubes was textured via chemical etching in a chemical bath of 1:1 solution of 12M hydrochloric acid and 3% hydrogen peroxide for 20 minutes at room temperature. The textured surfaces were functionalized by immersion in a chemical bath of 0.02 mol L^{-1} solution of n-hexadecyl mercaptan in ethanol at 60°C for one hour, to produce superhydrophobic surfaces (SHS). For fabrication of lubricant infused surfaces (LIS), the superhydrophobic surfaces were infused with the lubricant oil by dripping it on the inside of the tube surfaces and using compressed air to spread it evenly. Following that, lubricant-infused tubes were placed vertically for about 12 hours to get rid of

excess lubricant to obtain just-filled asperity structures. Copper tubes with smooth, superhydrophobic and lubricant-infused inner surfaces were used for surface characterization and fouling experiments.

The morphological characteristics of the different fabricated surfaces are detailed elsewhere [25], which the reader is referred to. The wettability characteristics of the surfaces were measured using a ramé hart goniometer to obtain the water contact angle and the contact angle hysteresis or sliding angle. Smooth surface, by virtue of absence of any significant roughness features and the inherent hydrophilic nature of copper, showed a lower contact angle value of 70° and a relatively high contact angle hysteresis of 22°. The fabricated superhydrophobic surfaces exhibited distinct multiscale texture with a peak-to-valley height, measured using a Dektak contact profilometer, of about 5–10 μm, and water contact angle value of about 157°, well in the excess of 150° that defines superhydrophobicity. The contact angle hysteresis was measured to be less than 2°, signifying exceptional nonwettability. Lubricant-infused surfaces inherited the roughness features of the base SHS spanning several length scales in which the asperity valleys were infused with Krytox 104. The hydrophobic slippery nature of the infused lubricant renders the surface hydrophobic in nature with contact angle of 124° and a relatively low sliding angle value of 12°.

The experimental setup for the fouling studies consisted of a convective heat transfer flow loop. The primary components of the system included a tank with an agitation pump and chiller loop, a centrifugal pump to circulate the scaling solution, a test section bypass line controlled by a ball valve, and the test section line controlled by a needle valve. The test section was heated by a heater jacket comprised of three, flexible, alternating current (AC) polyimide heaters connected to a variable, AC transformer. Instrumentation of the apparatus consisted of three Class A resistance temperature detectors with accuracy of $\pm$0.05°C for measuring test section inlet temperature (T_i), outlet temperature (T_o), and exterior wall temperature (T_w), as well as a magnetic flowmeter with accuracy of $\pm$0.5% for measuring volumetric flowrate ($\dot{V}$) through the test section. All gauge measurements were acquired and displayed using National Instruments temperature (NI-9216) and multifunction (NI-9381) input modules and LabView 2020.

Each fouling experiment consisted of flowing a supersaturated solution of calcium sulfate in water through the tube section with desired flow Reynolds number, and recording the inlet, outlet and the wall temperatures as a function of time. The experiment was considered complete when the wall temperature remained nearly invariant with time corresponding to the attainment of an asymptotic fouling on the inner tube surface. The additional thermal resistance due to the deposition of the minerals, termed the fouling resistance (R_f), was calculated from the measured temperature and volumetric flow rate, the thermophysical properties of the solution (density, ρ, and specific heat, c_p), and the inner surface area of the tube, A_s, as:

$$R_f = \frac{A_s}{\rho \dot{V} c_p \ln\left(\frac{T_w - T_o}{T_w - T_i}\right)} - R_T^0 \tag{1}$$

in which, R_T^0 is the unfouled resistance corresponding to the case of flow of water without the presence of any fouling agent. After the fouling experiment, the test section was removed from the apparatus and allowed to dry for 24 hours before preparing for SEM imaging.

Fouling studies were conducted for combinations of the four parameters—surface type (smooth, SHS and LIS), foulant temperature, T (taken to be the same as the inlet temperature to the test section, T_i), Reynolds number, Re, defined in terms of the tube diameter, and the dimensionless foulant concentration, c/s—where s is the solubility of calcium sulfate in water, $s = 2.6 \times 10^{-3}$ g/ml. The experiments were conducted for Re = 1000, 2000, and 3000, T = 293 K, 303 K, 313 K, and 323 K, and c/s = 2.0, 2.5 and 3.0. In a uniquely novel approach, the different discrete surface types are studied in a unified way through the ratio of the infused lubricant viscosity (μ_l) to that of the flowing fluid (μ_w). In this representation, $\mu_l/\mu_w = 0$ denotes SHS with air-filled asperity, $\mu_l/\mu_w \to \infty$ represents a smooth solid (equivalent to the asperity valleys being infused by the base solid material of infinite viscosity), and all lubricant-infused surfaces correspond to finite values of the viscosity ratio, $0 < \mu_l/\mu_w < \infty$, as follows: Krytox 102 LIS—28; Krytox 103 LIS—58; Krytox 104 LIS—110; and Krytox 105 LIS—310. The results of the experimental studies are described in the next section.

3. RESULTS AND DISCUSSION

Figure 1 shows a set of scanning electron microscope (SEM) images of (a) smooth, (b) superhydrophobic and (c) lubricant-infused surfaces at the end of calcium sulfate fouling experiments. In order to elucidate the interaction mechanism of calcium sulfate foulant with all three surface types, regions of foulant deposition are shown at two different magnifications for each surface. Collectively, Figure 1a-c reveals that calcium sulfate foulant deposits in the form of mesh-like structures comprising smaller-scale fundamental needle shaped crystals, of an average width of around 1 μm. Figure 1a identifies regions of isolated needle shaped structures deposited onto the smooth homogeneous surface. The needle-shaped structures progressively form larger aggregates with subsequent deposition of more needle shaped structures, resulting in a complex interlocking mesh structure.

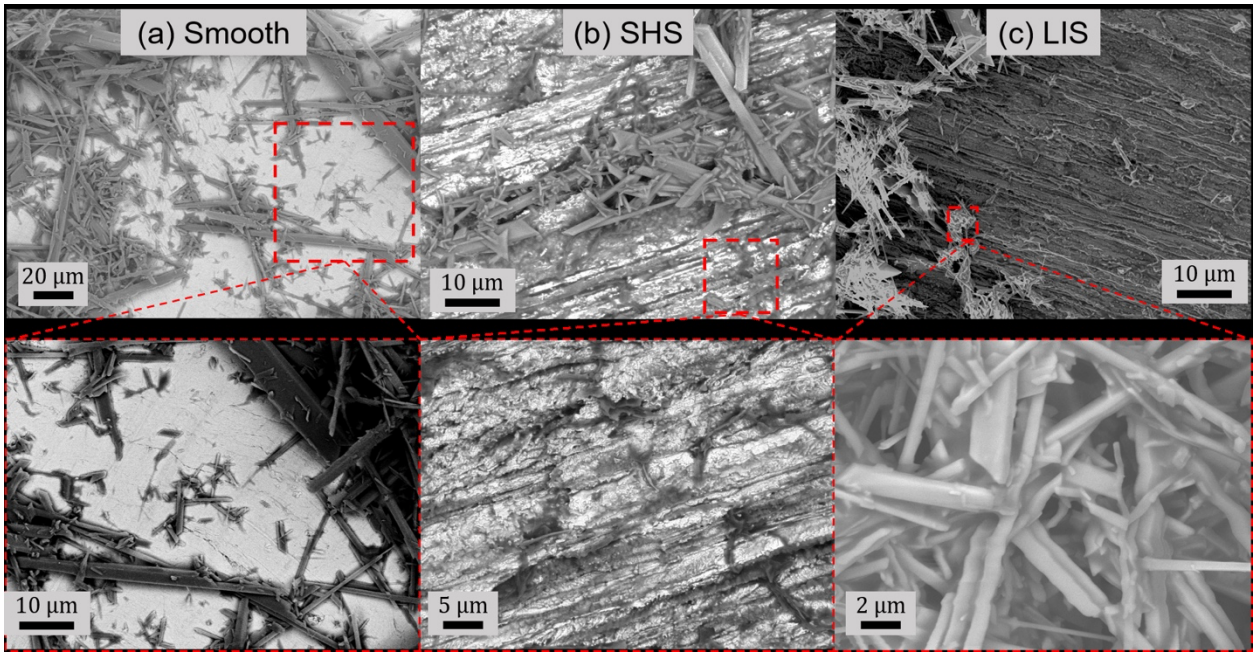

Figure 1: SEM images of foulant deposits on (a) smooth, (b) SHS and (c) Krytox 105 LIS, at two magnifications.

For superhydrophobic surfaces, the deposition of calcium sulfate offers two separate interaction mechanisms. From Figure 1b, it is evident that the length-scale of the interstitial spaces between the asperities is of the same order of the characteristic thickness of the calcium sulfate needles undergoing deposition. Therefore, in the case of superhydrophobic surfaces, needle

shaped foulant particles deposit deep within the asperity valleys as the foulant solution penetrates and wets the interstitial region, as seen from Figure 1b. In addition to the deposition of foulant within the voids, the simultaneous deposition onto the top of the asperities leads to larger effective area of foulant deposition resulting in relatively higher fouling of superhydrophobic surfaces compared to smooth surfaces, as later quantified with the heat transfer measurements. For lubricant-infused surfaces, the oil in the asperity valleys offers little nucleation of the foulant crystals leading to significantly diminished fouling, as evident from Figure 1c.

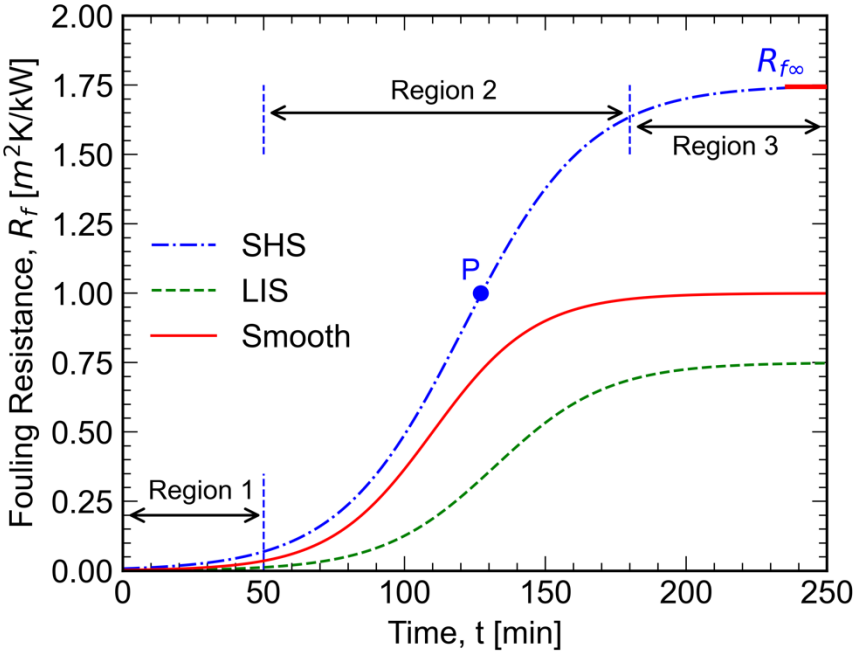

Figure 2: Time evolution of the fouling resistance for the three surface types.

Fouling on the different surfaces was further quantified by the fouling resistance as determined by Equation 1. Figure 2 presents the variation of fouling heat transfer resistance as a function of time for smooth, superhydrophobic and lubricant infused surfaces, exemplified by Krytox-105 as the infused lubricant. It is evident from Figure 2 that for all three surface types, the fouling resistance shows a monotonic increase with time, where the entire fouling behavior can be divided into three characteristic regions, as marked in Figure 2 for the case of SHS fouling. The first region is characterized by random nucleation and deposition of foulant particles in their

fundamental form/shape at various spots on the heat transfer surface. During this stage, the fouling thermal resistance shows insignificant change, as annotated as *Region 1* in Figure 2, and is termed as 'induction period' [26]. It is seen from Figure 2 that LIS has the longest induction period due to the reduced nucleation density on the lubricant surface and signifies deterrence of fouling deposition. In contrast, SHS has the shortest induction time denoting rapid onset of fouling. The performance of SHS is attributed to the removal of the air cushion in the asperity valleys by the flowing fluid that deteriorates the Cassie state of wettability responsible to superhydrophobicity to a Wenzel state and degrades the nonwetting characteristic. As a result, greater surface area is exposed on the asperities leading to the higher nucleation density and shorter induction time.

After the nucleation of foulant particles on heat transfer surfaces, the subsequent process of adhesion of foulant particles suspended in the solution results in the growth and spread of foulant deposits across the heat transfer surface leading to significant and rapid increase in heat transfer resistance values, depicted as *Region 2* in Figure 2. The first part of *Region 2*, up until the point of inflection (point P in Figure 2) is dominated by the adhesion of fresh foulant particles to the existing layer of foulant deposits, whereas in the part of *Region 2* after the inflection point, the shear exerted by the flowing foulant solution tends to take away the deposited layer of foulant leading to a decrease in the growth rate of the fouling resistance. It is seen in Figure 2 that *Region 2* is the steepest for SHS followed by smooth and LIS. The lowest growth rate for LIS in *Region 2* owes itself to the poor adhesion of the scalant minerals on the lubricant oil and reflects its superior anti-scaling characteristic compared to smooth and superhydrophobic surfaces.

With further progress of fouling the foulant deposition rate is balanced by the foulant removal rate governed by the shear from the flowing fluid, leading to a saturated value, called the asymptotic fouling resistance, $R_{f\infty}$, in *Region 3* of Figure 2. As a consequence of the longer (shorter) induction time in *Region 1* and the slower (faster) growth in *Region 2*, LIS (SHS) results in the least (greatest) value of $R_{f\infty}$ with the smooth surface exhibiting a value in between LIS and SHS. The variation of asymptotic fouling resistance in Figure 2 suggests a nonmonotonic trend among the surfaces, where $R_{f\infty}$ decreases from SHS ($\mu_l/\mu_w = 0$) to Krytox 105 LIS ($\mu_l/\mu_w = 310$) and increases as $\mu_l/\mu_w \to \infty$ (solid surface).

The nonmonotonic variation of $R_{f\infty}$ with the different surfaces, represented on a continuous spectrum in terms of the viscosity ratio, was explored in ref. [25] by conducting the fouling experiments on LIS infused with the four different Krytox oils spanning a viscosity ratio from 58 to 310, as mentioned in Section 2. The results from [25] are presented in Figure 3 for continuity of discussion, along with the asymptotic fouling resistance of smooth surface and SHS, which demonstrate that $R_{f\infty}$ initially decreases from SHS ($\mu_l/\mu_w = 0$) to Krytox 102 LIS ($\mu_l/\mu_w = 28$) due to the lower nucleation density on the lubricant oil. However, the lower viscosity of the infused lubricant, $\mu_l/\mu_w = 28$, causes partial lubricant drainage easily resulting in a reduction in $R_{f\infty}$ of about 0.25 m²K/kW (about 14.3%) with respect to SHS. As the lubricant viscosity increases the asymptotic fouling resistance of Krytox 103 LIS ($\mu_l/\mu_w = 58$), Krytox 104 LIS ($\mu_l/\mu_w = 110$), and Krytox 105 LIS ($\mu_l/\mu_w = 310$) show progressively lower values of $R_{f\infty}$ for a reduction of as much as 1 m²K/kW (about 57.1%) with respect to SHS such for Krytox 105 LIS. With further increase in the viscosity ratio towards ∞, the smooth surface, the asymptotic fouling resistance approaches a value of 1 m²K/kW. This suggests that fouling resistance can be minimized by appropriately tailoring the LIS; based on the data presented in Figure 3, Krytox 105 LIS with a viscosity ratio of 310 is seen to yield the minimum $R_{f\infty}$. Further, an improperly designed LIS with a low viscosity oil would, in fact, lead to worse fouling resistance than the smooth surface.

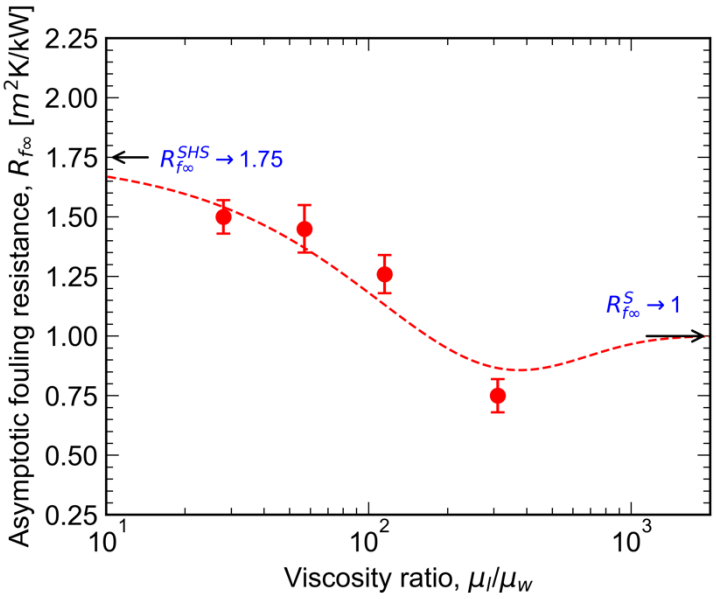

Figure 3: Variation of the asymptotic fouling resistance with surface type, parametrized in terms of the viscosity ratio, for $Re = 2000$, $c/s = 2.5$, and $T = 293$ K (after [25]).

The nonmonotonic variation of the asymptotic fouling resistance with viscosity ratio was described mathematically in ref. [25] as:

$$R_{f\infty} = R_{f\infty}^{S}\left(1 - e^{-\frac{1}{\delta}\frac{\mu_l}{\mu_w}}\right) + R_{f\infty}^{SHS} e^{-\frac{2}{\delta}\frac{\mu_l}{\mu_w}} \quad (2)$$

where $R_{f\infty}^{S}$ and $R_{f\infty}^{SHS}$ are the asymptotic fouling resistance for smooth and superhydrophobic surfaces, respectively, and δ is a positive constant. Equation 2 satisfies several physical consistency checks, as explained in ref. [25]. While the above equation captures the relationship of the asymptotic fouling resistance with the surface type, parametrized in terms of the viscosity ratio, fouling is also dependent on the Reynolds number (Re), foulant concentration (c/s) and temperature (T), which arise from the dependencies of $R_{f\infty}^{S}$ and $R_{f\infty}^{SHS}$ themselves on the three parameters that need to be understood. To this end, Figures 4a, 4b and 4c present the variation of $R_{f\infty}^{S}$ and $R_{f\infty}^{SHS}$ with Re and c/s and T, respectively, keeping constant the values of the other two parameters than the one being examined.

Figures 4a–c indicate that for any combination of Re, c/s, and T the superhydrophobic surface yields higher asymptotic fouling resistance compared to the smooth surface, owing to the penetration of foulant solution deep within the asperities on SHS as discussed earlier. From Figure 4a, it is evident that for both smooth surface and SHS, the asymptotic fouling resistance decreases monotonically with increase in Reynolds number. Increase in Reynolds number increases the shear exerted by the flowing fluid resulting in higher rate of foulant removal leading to lower asymptotic fouling resistance. Figure 4b reveals a monotonic increase of the asymptotic fouling resistance with dimensionless concentration, for both smooth surface and SHS. An increase in the foulant concentration in solution directly increases the driving force for fouling, leading to increased $R_{f\infty}^{S}$ and $R_{f\infty}^{SHS}$ values. The monotonic variations with Re and c/s may be described by power-law relationships, as explained in ref. [25].

The variation of the asymptotic fouling resistance with temperature is presented in Figure 4c on a semi-log plot with the inverse of the absolute temperature ($1/T$) and depicts an increase in $R_{f\infty}^{S}$ and $R_{f\infty}^{SHS}$ with temperature. The increase in asymptotic fouling resistance with temperature is attributed to two physical phenomena. First, with increase in foulant temperature, the solubility of mineral salts such as calcium sulfate decreases [27] leading to the availability of higher amount

of undissolved salt for deposition on heat transfer surfaces. Secondly, with increase in temperature, the interfacial tension of water decreases leading to increased adhesion of foulant solution to heat transfer surfaces. However, with further increase in temperature, the effects of decreasing foulant solubility and increasing adhesion and spreading of foulant onto heat transfer surfaces diminish, and the asymptotic fouling resistance reaches a maximum value corresponding to the intercepts on the ordinate. It is evident from the plot that for both smooth surface and SHS, the asymptotic fouling resistance varies linearly on the semi-log plot, suggesting and Arrhenius temperature dependence.

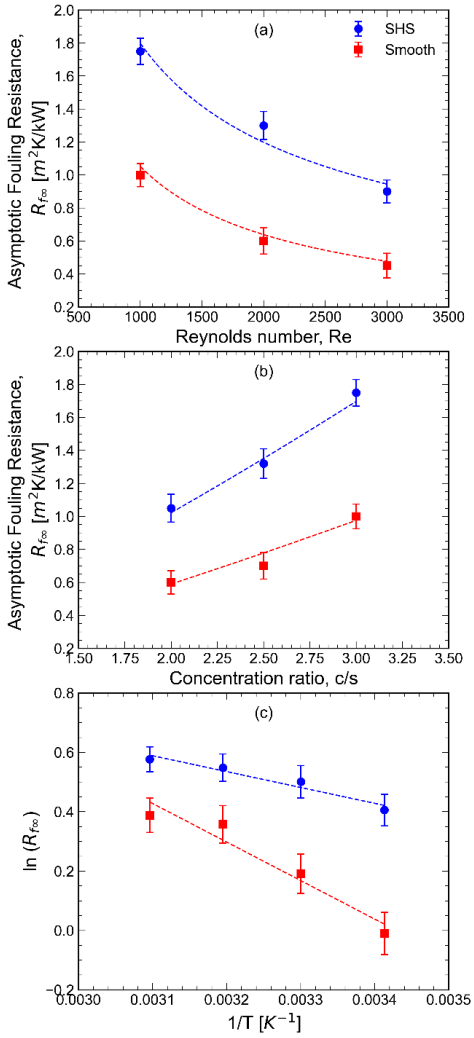

Figure 4: Variation of asymptotic fouling resistance for smooth surface and SHS with (a) Reynolds number ($c/s = 2.5$ and $T = 293$ K), (b) dimensionless concentration ($Re = 2000$ and $T = 293$ K), and (c) temperature ($Re = 2000$ and $c/s = 2.5$).

Based on the parametric variations seen in Figure 4a–c, the asymptotic fouling resistance of smooth surface and SHS may be expressed in terms of $Re, c/s$, and T as a combination of power-law and Arrhenius relationships given by $R_{f\infty}^{S} = A_S e^{-\frac{T_S^*}{T}} Re^{-a_S} \left(\frac{c}{s}\right)^{b_S}$ and $R_{f\infty}^{SHS} = A_{SHS} e^{-\frac{T_{SHS}^*}{T}} Re^{-a_{SHS}} \left(\frac{c}{s}\right)^{b_{SHS}}$, in which $A_S, a_S, b_S, T_S^*, A_{SHS}, a_{SHS}, b_{SHS}$, and T_{SHS}^* are all positive constants and the subscripts S and SHS refer to smooth and superhydrophobic surfaces, respectively. Substituting these relationships in Equation 2, we obtain the following analytical model for the asymptotic fouling resistance of any surface type, SHS, LIS or smooth surface, in a unified manner:

$$R_{f\infty} = A_S e^{-\frac{T_S^*}{T}} Re^{-a_S} \left(\frac{c}{s}\right)^{b_S} \left(1 - e^{-\frac{1}{\delta}\frac{\mu_l}{\mu_w}}\right) + A_{SHS} e^{-\frac{T_{SHS}^*}{T}} Re^{-a_{SHS}} \left(\frac{c}{s}\right)^{b_{SHS}} e^{-\frac{2}{\delta}\frac{\mu_l}{\mu_w}} \quad (3)$$

The above equation correctly represents the physical behavior and satisfies several limit checks, that the asymptotic fouling resistance tends to zero as $Re \to \infty$ or $c/s \to 0$, and conversely, that the asymptotic fouling resistance becomes very large as $Re \to 0$ (static fouling) or $c/s \to \infty$.

Equation 3 involves 9 constants—$\delta, A_S, a_S, b_S, T_S^*, A_{SHS}, a_{SHS}, b_{SHS}$, and T_{SHS}^*—of which δ, a_S, b_S, a_{SHS}, and b_{SHS} are adopted from the detailed study of the effects of Reynolds number, foulant concentration and viscosity ratio reported in ref. [25]. The terms T_S^* and T_{SHS}^* in the Arrhenius exponent are obtained as the magnitude of the slopes of the best-fit linear fits through the data in Figure 4c. Finally, the constants A_S and A_{SHS} are determined such that $A_S e^{-\frac{T_S^*}{T}}$ and $A_{SHS} e^{-\frac{T_{SHS}^*}{T}}$ evaluated at $T = 293$ K correspond to the power-law coefficients 5 and 2.5, respectively, reported in ref. [25] for a foulant temperature of 293 K. Table 1 summarizes the values of the 9 constants in the unified relationship for the asymptotic fouling resistance.

Table 1: Constants in Equation 3

A_S	a_S	b_S	T_S^* [K]	δ	A_{SHS}	a_{SHS}	b_{SHS}	T_{SHS}^* [K]
419	0.68	3.14	1300	240	15	0.50	3	534

The accuracy of the unified analytical relationship, Equation 3, was assessed by comparing the model predictions with experimentally obtained values of asymptotic fouling resistance for a wide range of parameter combinations. The results are presented in Figure 5 where the diagonal

line corresponds to an exact agreement between the model and experimental values, and the dashed and chain-dashed lines denote the 10% and 20% error bounds. The experimental data comparison includes the 8 cases in Figure 4c covering four temperatures for smooth surface and SHS, 29 cases borrowed from [25] spanning Reynolds number of 1000, 2000, and 3000, concentration ratio of 2.0, 2.5 and 3.0, and six surface types (smooth, SHS, and four LIS), and 11 cases from Lee et al. [28], as identified in Figure 5. Lee et al. [28] reported calcium sulfate scaling on chevron-patterned heat transfer surfaces in terms of the chevron angle. The data was extrapolated for the case of 0° angle to correspond to a smooth case and used in the comparison. An additional 13 fouling experiments were conducted in this study for various parametric combinations of Reynolds number, calcium sulfate concentration ratio, temperature and six surface types parametrized in terms of the viscosity ratio, as listed in Table 2. In all, a total of 61 experimental data are presented for the validation in Figure 5.

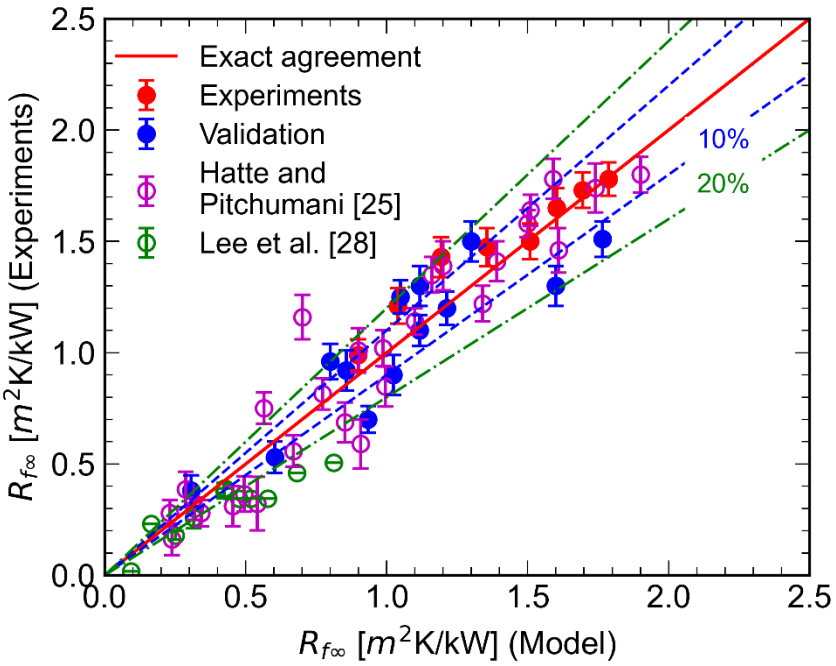

Figure 5: Comparison of the model predictions of asymptotic fouling resistance (Equation 3) with a comprehensive set of experimental data.

It is evident from Figure 5 that the experimental data shows a good agreement with the model. Out of 8 experimental data points that represent the variation of temperature in the present study,

a total of 7 data points fall within 10% error bounds and all 8 experiments are predicted within 20% error bounds. For the set of 13 validation experiments, 10 experiments are predicted with less than 10% error and all are predicted within 20% error bounds when compared against the current model. From the pool of 29 experimental data points borrowed from ref. [25] a total of 24 data points are observed to fall within the 10% error bounds and 27 data points are predicted within 20% error bounds. It is seen from Figure 5 that the experimental data obtained from Lee et al. [28] shows that 6 data points are predicted within 10% error bounds whereas the rest 5 data points are observed to fall slightly outside the 20% error bounds. It is noted that the experimental data from [28] are for various chevron angles that are reduced to an equivalent smooth surface by extrapolating the functional dependence of chevron angle on the asymptotic fouling resistance. Therefore, the uncertainty involved in the conversion of Lee et al. [28] data from non-zero chevron angles to equivalent smooth surface (zero chevron angle) is postulated to be the reason behind the some of the data points lying outside the 20% error bounds. Nevertheless, a total of 90% of the data pooled from various sources are predicted by the model to within 20%. Considering the inherent uncertainty in the fouling process, this represents an excellent level of accuracy of the presented model.

Table 2: Parametric combinations used for the experimental validation of the model.

Experiment no.	Reynolds number, Re	Foulant concentration c/s	Temperature [K]	Viscosity ratio μ_l/μ_w
1	2000	3.0	303	110
2	2000	3.0	313	110
3	2000	3.0	323	110
4	3000	2.0	313	58
5	3000	2.5	313	58
6	3000	3.0	313	58
7	1000	3.0	323	310
8	2000	3.0	323	310
9	3000	3.0	323	310
10	1000	2.5	303	0
11	1000	2.5	303	28
12	1000	2.5	303	310
13	1000	2.5	303	∞

The results presented so far point to LIS with an optimum tailoring of the lubricant viscosity could lead to minimum fouling resistance. The validated analytical relationship in Equation 3 provides for deriving the optimum surface design that yields a minimum asymptotic fouling resistance, thereby superior fouling performance. Setting the first derivative of $R_{f\infty}$ given by Equation 3 with respect to the viscosity ratio and setting it to zero, the optimum viscosity ratio $\left(\frac{\mu_l}{\mu_w}\right)^*$ is derived as a function of Reynolds number, concentration ratio and temperature:

$$\left(\frac{\mu_l}{\mu_w}\right)^* = \delta \ln\left[2\left(\frac{A_{SHS}}{A_S}\right) Re^{(a_S - a_{SHS})} \left(\frac{c}{s}\right)^{(b_{SHS} - b_S)} e^{\left(\frac{T_S^* - T_{SHS}^*}{T}\right)}\right] \tag{4}$$

and the corresponding minimum asymptotic fouling resistance is obtained by substituting Equation 4 in Equation 3 as:

$$R_{f\infty}^{min} = A_S Re^{-a_S} \left(\frac{c}{s}\right)^{b_S} e^{-\frac{T_S^*}{T}} \left[1 - 0.25\left(\frac{A_S}{A_{SHS}}\right) Re^{(a_{SHS} - a_S)} \left(\frac{c}{s}\right)^{(b_S - b_{SHS})} e^{\left(\frac{T_{SHS}^* - T_S^*}{T}\right)}\right] \tag{5}$$

The fouling mitigation performance of the optimum surface design yielding the minimum asymptotic fouling resistance can be compared to the case of a conventional smooth surface. To this end, a percentage fouling reduction relative to smooth surface is defined as $\Delta = \left(\frac{R_{f\infty}^S - R_{f\infty}^{min}}{R_{f\infty}^S}\right) \times 100\%$. Using $R_{f\infty}^{min}$ from Equation 5 and $R_{f\infty}^S$ defined previously, the percentage fouling reduction, Δ, is expressed as:

$$\Delta = 25\left(\frac{A_S}{A_{SHS}}\right) Re^{(a_{SHS} - a_S)} \left(\frac{c}{s}\right)^{(b_S - b_{SHS})} e^{\left(\frac{T_{SHS}^* - T_S^*}{T}\right)} \tag{6}$$

Figures 6 and 7 present contours of optimum viscosity ratio (Equation 4), the corresponding minimum fouling resistance (Equation 5) and the percentage fouling reduction relative to smooth surface (Equation 6) as a function of Reynolds number and temperature, for $c/s = 2.0$ and $c/s = 3.0$, respectively. Figures 6a and 7a show that for a fixed Re and c/s, the optimum viscosity ratio decreases with increase in foulant temperature. With increase in temperature, the propensity for fouling increases, which is mitigated by a lower viscosity lubricant than a higher viscosity (solid-like) lubricant. Likewise, increasing c/s also increases the tendency for scaling, and it is seen from a comparison of Figures 6a and 7a, that the optimum viscosity ratio decreases with increasing foulant concentration, for the same Reynolds number and temperature. The corresponding minimum fouling resistance increases with increase in foulant temperature or foulant

concentration ratio, as seen from Figures 6b and 7b. Further, for a fixed temperature and concentration ratio, Figures 6a and 7a show that increasing the Reynolds number requires a higher viscosity LIS to withstand the higher shear by the flowing fluid, as reflected in the increasing $\left(\frac{\mu_l}{\mu_w}\right)^*$ with Re. The corresponding minimum fouling resistance decreases with increase in Reynolds number owing to the increased shear on the surface by the flow.

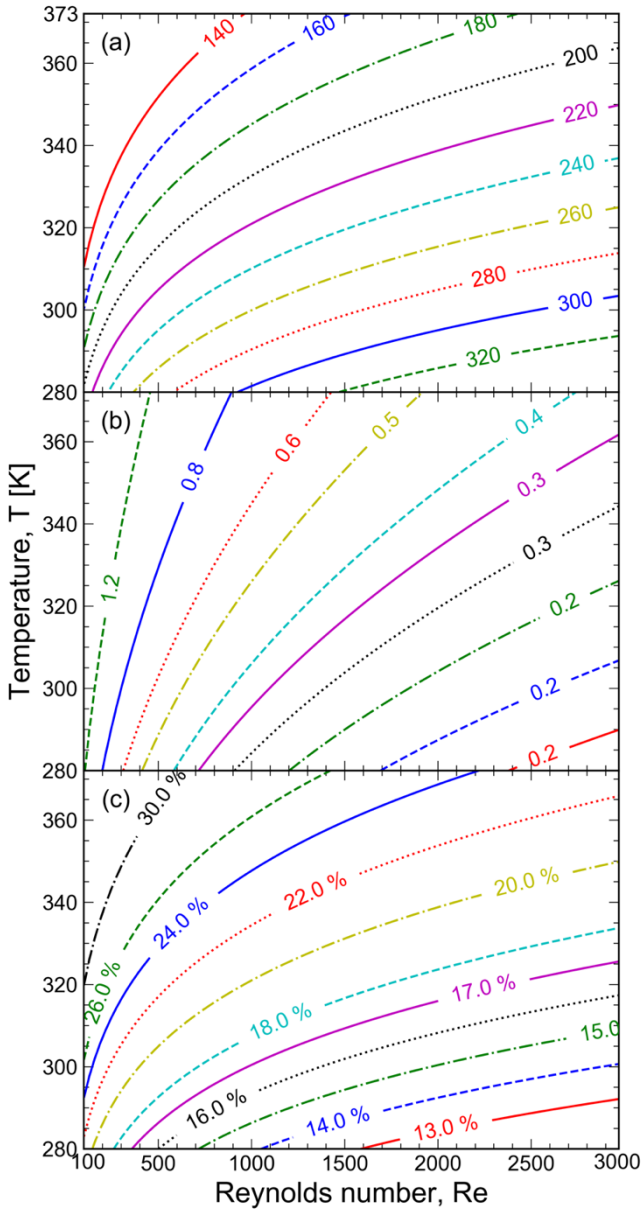

Figure 6: Contour maps of (a) optimum LIS design in terms of $\left(\frac{\mu_l}{\mu_w}\right)^*$, (b) the minimum asymptotic fouling resistance, $R_{f\infty}^{min}$, and (c) percentage fouling reduction, Δ, as function of Reynolds number and temperature, for $c/s = 2.0$.

Figures 6c and 7c demonstrate that the percentage fouling reduction, Δ, achieved using the optimal LIS design is greater for low Reynolds number, high temperature and high foulant concentration, all conditions that promote increased fouling. Figures 6c and 7c show that, in the range of parameters studied, Δ of at least ~12% and up to 30% or more can be realized through the use of optimally tailored LIS. The synergistic increase in the percentage fouling reduction with conditions that lead to greater fouling on conventional surfaces points to the superior advantage of the nonwetting surfaces in mitigating fouling.

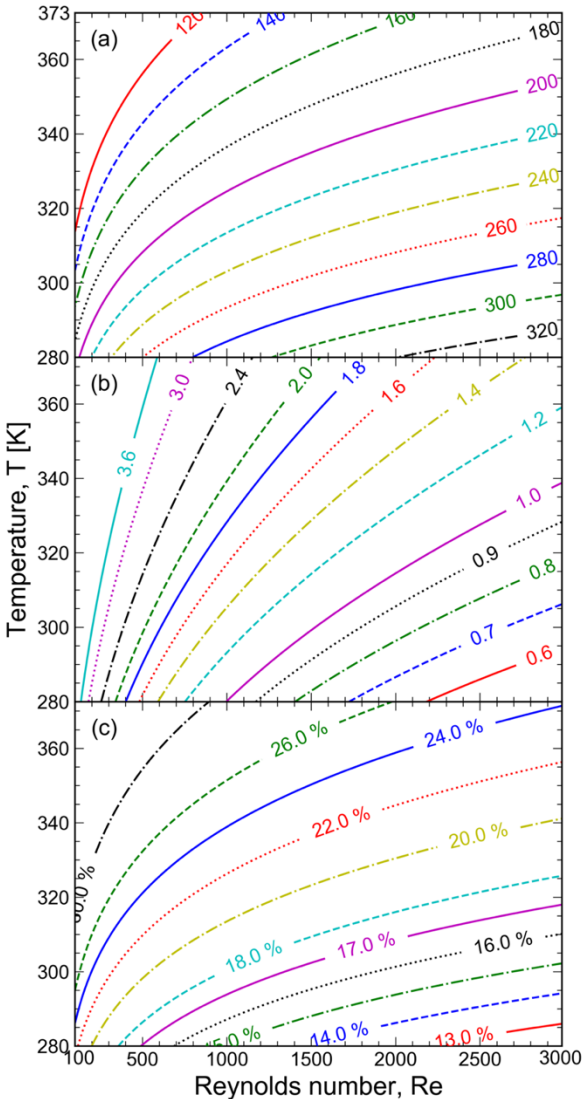

Figure 7: Contour maps of (a) optimum LIS design in terms of $\left(\frac{\mu_l}{\mu_w}\right)^*$, (b) the minimum asymptotic fouling resistance, $R_{f\infty}^{min}$, and (c) percentage fouling reduction, Δ, as function of Reynolds number and temperature, for $c/s = 3.0$.

CONCLUSIONS

The study presented, for the first time, a unified approach to compare temperature-dependent calcium sulfate heat transfer fouling performance of smooth, superhydrophobic and lubricant-infused surfaces. Using a forced convection experimental setup, the time evolution of fouling was quantified and shown to be higher for superhydrophobic surface compared to conventional smooth surface; Krytox 105 lubricant-infused surface, on the other hand, demonstrated lower fouling resistance throughout. In a uniquely novel approach, the discrete surface types were represented on a continuous spectrum in terms of a viscosity ratio of the infused fluid to the flowing fluid. It was shown that the asymptotic fouling resistance exhibits a nonmonotonic variation with respect to the surface type suggesting that the surface can be tailored to minimize fouling. Through a systematic set of experiments, a unified analytical model was developed for the evaluation of asymptotic fouling resistance based on the Reynolds number, foulant concentration, temperature, and surface types. The model is shown to compare well with experimental data from this study as well as from the literature. The unified formulation was then used to develop design maps for determining optimum nonwetting surface designs for minimizing asymptotic fouling resistance as function of temperature, Reynolds number and foulant concentration. It was shown that optimally tailored surfaces yield up to 30% or more in fouling reduction compared to conventional smooth surfaces. The results of the study present, for the first time, a rational approach to design of engineered anti-fouling nonwetting surfaces that can be translated to practice.

ACKNOWLEDGEMENT AND DISCLAIMER

The material reported in this publication is based upon work supported by the U.S. Department of Energy under Award Number DE-FE0031556. This publication was prepared as an account of work sponsored by an agency of the United States Government. Neither the United States Government nor any agency thereof, nor any of their employees, makes any warranty, express or implied, or assumes any legal liability or responsibility for the accuracy, completeness, or usefulness of any information, apparatus, product, or process disclosed, or represents that its use would not infringe on privately owned rights. Reference herein to any specific commercial

product, process, or service by trade name, trademark, manufacturer, or otherwise does not necessarily constitute or imply its endorsement, recommendation, or favoring by the United States Government or any agency thereof. The views and opinions of authors expressed herein do not necessarily state or reflect those of the United States Government or any agency thereof.

REFERENCES

[1] C.H. Chen, Q. Cai, C. Tsai, C.L. Chen, G. Xiong, Y. Yu, Z. Ren, Dropwise condensation on superhydrophobic surfaces with two-tier roughness, Appl. Phys. Lett. 90 (2007) 2005–2008, doi: 10.1063/1.2731434 .

[2] N. Miljkovic, E.N. Wang, Condensation heat transfer on superhydrophobic surfaces, MRS Bull 38 (2013) 397–406, doi: 10.1557/mrs.2013.103 .

[3] R. Stoddard, K. Nithyanandam and R. Pitchumani, Steam Condensation Heat Transfer on Lubricant-infused Surfaces, IScience. 24 (2021) 102336. doi:10.1016/j.isci.2021.102336.

[4] A. R. Betz, J. Jenkins, C.J. Kim, D. Attinger, Boiling heat transfer on super- hydrophilic, superhydrophobic, and superbiphilic surfaces, Int. J. Heat Mass Transf. 57 (2013) 733–741, doi: 10.1016/j.ijheatmasstransfer.2012.10.080.

[5] D. Maynes, B. W. Webb and J. Davies, Thermal Transport in a Microchannel Exhibiting Ultrahydrophobic Microribs Maintained at Constant Temperature, J. Heat Transfer. 130 (2008) 1–8. doi:10.1115/1.2789715.

[6] S. Hatte and R. Pitchumani, Analysis of Laminar Convective Heat Transfer Over Structured Non-Wetting Surfaces, Int. J. Heat Mass Transf. 167 (2021) 120810. doi:10.1016/j.ijheatmasstransfer.2020.120810.

[7] D. Moreira, and P. R. Bandaru, Thermal transport in laminar flow over superhydrophobic surfaces, utilizing an effective medium approach. Phys. of Fluids *27 (5)* (2015) 052001. doi.org/10.1063/1.4919699.

[8] S. Hatte and R. Pitchumani, Analysis of Convection Heat Transfer on Multiscale Rough Superhydrophobic and Liquid Infused Surfaces. Chemical Engineering Journal 424 (2021): 130256. doi:10.1016/j.cej.2021.130256

[9] B.R. Solomon, K.S. Khalil, K.K. Varanasi, Drag reduction using lubricant- impregnated surfaces in viscous laminar flow, Langmuir 30 (2014) 10970–10976, doi: 10.1021/la5021143.

[10] S. Hatte and R. Pitchumani, Analytical Model for Drag Reduction on Liquid-infused Structured Non-wetting Surfaces. Soft Matter 17(5) (2021): 1388-1403. doi:10.1039/D0SM01272F

[11] H. Dong, M. Cheng, Y. Zhang, H. Wei, F. Shi, Extraordinary drag-reducing effect of a superhydrophobic coating on a macroscopic model ship at high speed, J. Mater. Chem. A. 1 (2013) 5886–5891, doi: 10.1039/c3ta10225d.

[12] S. Hatte and R. Pitchumani, Fractal Model for Drag Reduction on Multiscale Nonwetting Rough Surfaces. Langmuir 36, no. 47 (2020): 14386–14402. doi: 10.1021/acs.langmuir.0c02790.

[13] J. Ou, B. Perot, J.P. Rothstein, Laminar drag reduction in microchannels using ultrahydrophobic surfaces, Phys. of Fluids. 16 (2004) 4635–4643, doi: 10.1063/ 1.1812011.

[14] T. B. Nguyen, S. Park and H. Lim, Effects of Morphology Parameters on Anti-icing Performance in Superhydrophobic Surfaces, Appl. Surf. Sci. 435 (2018) 585–591. doi:10.1016/j.apsusc.2017.11.137.

[15] M. Ruan, W. Li, B. Wang, B. Deng, F. Ma and Z. Yu, Preparation and Anti-icing Behavior of Superhydrophobic Surfaces on Aluminum Alloy Substrates, Langmuir. 29 (2013) 8482–8491. doi:10.1021/la400979d.

[16] K. Nithyanandam, P. Shoaei and R. Pitchumani, Technoeconomic Analysis of Thermoelectric Power Plant Condensers with Nonwetting Surfaces. Energy 227 (2021) 120450. doi:10.1016/j.energy.2021.120450

[17] D. Q. Kern and R. E. Seaton, A Theoretical Analysis of Thermal Surface Fouling, Br. Chem. Eng., vol. 4, no. 5, pp. 258-262, 1959.

[18] M.E. Walker, I. Safari, R.B. Theregowda, M.K. Hsieh, J. Abbasian, H. Arastoopour, D.A. Dzombak and D.C. Miller, Economic Impact of Condenser Fouling in Existing Thermoelectric Power Plants, Energy 44 (2012) 429–437. doi:10.1016/j.energy.2012.06.010.

[19] P. Zhang, L. Lin, D. Zang, X. Guo and M Liu, Designing Bioinspired Anti-Biofouling Surfaces based on a Superwettability Strategy. Small, 13(4) (2017) 1503334. doi:10.1002/smll.201503334

[20] M. Ferrari, and A. Benedetti, Superhydrophobic Surfaces for Applications in Seawater. Advances in colloid and interface science, 222 (2015) 291-304. doi:10.1016/j.cis.2015.01.005

[21] J. Genzer, and K. Efimenko, Recent Developments in Superhydrophobic Surfaces and Their Relevance to Marine Fouling: a Review. Biofouling, 22 (5) (2006) 339-360. doi:10.1080/08927010600980223

[22] M. Ferrari, A. Benedetti, E. Santini, F. Ravera, L. Liggieri, E. Guzman and F. Cirisano, Biofouling Control by Superhydrophobic Surfaces in Shallow Euphotic Seawater. Colloids and Surfaces A: Physicochemical and Engineering Aspects, 480 (2015) 369-375. doi:10.1016/j.colsurfa.2014.11.009.

[23] S. B. Subramanyam, G. Azimi and K. K. Varanasi, Designing Lubricant-Impregnated Textured Surfaces to Resist Scale Formation. Advanced Materials Interfaces, 1 (2) (2014) 1300068. doi:10.1002/admi.201300068

[24] W. Jiang, J. He, F. Xiao, S. Yuan, H. Lu and B. Liang, Preparation and Antiscaling Application of Superhydrophobic Anodized CuO Nanowire Surfaces. Industrial & Engineering Chemistry Research, 54(27) (2015) 6874-6883. doi:10.1021/acs.iecr.5b00444

[25] S. Hatte and R. Pitchumani, Generalized Analysis of Dynamic Flow Fouling on Heat Transfer Surfaces. International Journal of Heat and Mass Transfer, 188 (2022) 122573. doi.org/10.1016/j.ijheatmasstransfer.2022.122573

[26] H. Müller-Steinhagen, Cooling-Water Fouling in Heat Exchangers. Advances in Heat Transfer, 33 (1999) 414:496. doi.org/10.1016/S0065-2717(08)70307-1.

[27] W. Ma, Z. Wang, F. Jiao, Y. Zhen and C. Ma Study on Fouling Characteristics of CaCO3 at Low Reynolds Number. Environmental Progress & Sustainable Energy 38.5 (2019): 13163. doi:10.1002/ep.13163

[28] E. Lee, J. Jeon, H. Kang and Y. Kim, Thermal Resistance in Corrugated Plate Heat Exchangers Under Crystallization Fouling of Calcium Sulfate (CaSO4). International

Journal of Heat and Mass Transfer 78 (2014): 908-916. doi:10.1016/j.ijheatmasstransfer.2014.07.069